Breakthrough dynamics of nitrogen, oxygen, and argon on silver exchanged titanosilicates (Ag-ETS-10)

Sayed Alireza Hosseinzadeh Hejazi[1] · Libardo Estupiñan Perez[2] · Rafael Teruo Maruyama[2] · Arvind Rajendran[2] · Steven M. Kuznicki[2]

Abstract

Breakthrough curves of N_2, O_2, and Ar on Silver exchanged titanosilicates (Ag-ETS-10) extrudates and granules were measured using a laboratory scale dynamic column breakthrough (DCB) apparatus. In order to investigate the dynamics of the mass transfer, effect of flow rate, temperature and pressure on the composition and temperature curves were studied. In a separate attempt, N_2 breakthrough curves on two columns filled with Ag-ETS-10 extrudates and granules with two different sizes were obtained. Influence of axial-dispersion, macropore, and film resistance within the column was investigated using fundamentals of mass transfer and fluid dynamics which assisted in classifying the dynamics of this separation. The experimental results indicated the rapid mass transfer and the potential for rapid cycles using Ag-ETS-10 for high-purity O_2 production. A fully predictive mathematical model was shown to describe the experimental curves to a high level of precision.

Keywords Breakthrough experiment · Oxygen purification · Air separation · Titanosilicates

Abbreviations

b	Parameter in Langmuir isotherm ($m^3\,mol^{-1}$)
b_0	Parameter in Langmuir isotherm ($m^3\,mol^{-1}$)
c	Fluid phase concentration ($mol\,m^{-3}$)
C_{pa}	Specific heat capacity of the adsorbed phase ($J\,mol^{-1}\,K^{-1}$)
C_{pg}	Specific heat capacity of the gas phase ($J\,mol^{-1}\,K^{-1}$)
C_{ps}	Specific heat capacity of the adsorbent ($J\,kg^{-1}\,K^{-1}$)
C_{pw}	Specific heat capacity of the column wall ($J\,kg^{-1}\,K^{-1}$)
d	Parameter in dual-site Langmuir isotherm ($m^3\,mol^{-1}$)
d_0	Parameter in dual-site Langmuir isotherm ($m^3\,mol^{-1}$)
D_L	Axial dispersion ($m^2\,s^{-1}$)
D_m	Molecular diffusivity ($m^2\,s^{-1}$)
D_p	Macropore diffusivity ($m^2\,s^{-1}$)
d_p	Particle diameter (m)
F_{in}	Inlet flow rate (ccm)
F_{out}	Outlet flow rate (ccm)
h_{in}	Inside heat transfer coefficient ($J\,m^{-2}\,K^{-1}\,s^{-1}$)
h_{out}	Outside heat transfer coefficient ($J\,m^{-2}\,K^{-1}\,s^{-1}$)
k_i	Mass transfer coefficient (s^{-1})
k_f	External film resistance coefficient (s^{-1})
K_w	Thermal conductivity of column wall ($J\,m^{-1}\,K^{-1}\,s^{-1}$)
K_z	Effective gas thermal conductivity ($J\,m^{-1}\,K^{-1}\,s^{-1}$)
L	Column length (m)
L_p	Particle length (m)
M_{ads}	Mass of adsorbent (kg)
P	Pressure (Pa)
Pe	Peclet number
q	Solid phase concentration ($mol\,kg^{-1}$)
q_s	Saturation concentration in the solid phase ($mol\,kg^{-1}$)
q^*	Equilibrium solid phase concentration ($mol\,kg^{-1}$)
R	Universal gas constant ($Pa\,m^3\,mol^{-1}\,K^{-1}$)
r_{in}	Column inner radius (m)
r_{out}	Column outer radius (m)
r_p	Particle radius (m)

✉ Sayed Alireza Hosseinzadeh Hejazi
a.hejazi@aut.ac.ir

1 Department of Chemical Engineering, Amirkabir University of Technology (Tehran Polytechnic), No. 350, Hafez Ave, Valiasr Square, 1591634311 Tehran, Iran

2 Department of Chemical and Materials Engineering, University of Alberta, Donadeo Innovation Centre for Engineering, 9211-116 Street NW, Edmonton T6G 1H9, Alberta, Canada

Re	Reynolds number
Sc	Schmidt number
Sh	Sherwood number
T	Temperature (K)
T_a	Ambient temperature (K)
T_{bath}	Water bath temperature (K)
T_w	Column wall temperature (K)
t	Time (s)
U	Internal energy (J mol^{-1})
v	Interstitial velocity (m s^{-1})
V_b	Bed volume (m^3)
V_d	Dead volume (m^3)
y	Gas phase composition
z	Axial coordinate (m)

Greek symbols

ϵ	Bed voidage
ϵ_p	Particle voidage
μ	Fluid viscosity (kg m^{-1}s^{-1})
ρ_s	Adsorbent particle density (kg m^{-3})
ρ_w	Wall density (kg m^{-3})
τ	Tortuosity

Subscripts

avg	Average
in	Inlet stream
out	Outlet stream

1 Introduction

The demand for portable oxygen concentrators (POC) is growing worldwide [1, 2]. The rise in the number of patents and articles on portable medical oxygen concentrators, specifically by Sircar et al., in the recent years reflects the interest in developing new materials as well as adsorption processes to purify oxygen from air [3–7]. In addition to this, industries such as aerospace, semiconductors, military, and medical require the production of on-site oxygen with ultra-high purity (> 99.5%) [8]. It has been demonstrated that adsorption processes offer more favorable process economics as well as meeting the purity and throughput requirements for small-scale O$_2$ purification [9]. The aim of designing more efficient separation processes that can achieve high O$_2$ purities, entails the discovery of new adsorbent materials and novel design and development of highly-efficient pressure swing adsorption (PSA) processes. For instance, rapid pressure swing adsorption (RPSA) cycles can assist in improving the productivity of the desired component subjected to negligible mass transfer resistance in the adsorbent particles. In order to design efficient processes, a thorough understanding of the physical properties of the material,

adsorption mechanism, momentum, heat, and mass transfer mechanisms of the separation should be attained.

Our previous study showed that silver-exchanged titanosilicate (Ag-ETS-10) has the ability to purify oxygen in excess of 99.0% using a simple Skarstrom cycle [10]. Rigorous multi-objective optimizations to achieve high-purity oxygen productivity while minimizing total energy consumption of the process indicated the potential of Ag-ETS-10 for high purity oxygen separation using single- and dual-stage cycle configuration. It has been shown that 82.0% recovery for a product with a O$_2$ purity of 99.5% can be achieved using a 6-step cycle with heavy product pressurization and pressure equalization steps [10, 11]. In an experimental attempt, a product with O$_2$ purity of 98.3% and 10.6% recovery was obtained using Skarstrom cycle and the experimental profiles were predicted by the model in a satisfactory manner. Although our mathematical model was validated through single and multi-component DCB experiments [12], the purpose here is to provide a full description of the governing mechanisms for this process and verify the validity of the assumptions made. It has been pointed out that assumptions such as lumped mass and heat transfer coefficients require full experimental evidence and validation of the ability of the model to capture all the transport resistances in only one coefficient [13–15]. The literature shows that axial-dispersion could be the limiting mechanism in small scale high-purity O$_2$ production and neglecting this effect results in erroneous simulations and overestimation of the mass transfer coefficient in RPSA processes [16, 17]. Further, the study of operating conditions such as the flow rate, temperature, pressure, and particle size provides a full insight about the process dynamics and the conditions that favor the separation as well as identifying the governing transport mechanisms. For instance, particle size studies offer the necessary information about the dominant mass transfer resistance (micropore or macropore) in the adsorbent as well as the channeling and clustering within the column that can cause pressure drop and axial dispersion [2, 15].

We aim here at investigating the potential of Ag-ETS-10 as an effective adsorbent for high-purity oxygen production under RPSA cycles. Very few studies in the field of breakthrough research consider a well-organized procedure to identify the controlling physical phenomena. We suggest here a systematic approach to eliminate/confirm contributions from various mechanisms. In order to better understand the dynamics of the separation and the mechanisms that control the process, a series of experiments using an in-house DCB apparatus were carried out and the effect of flow rate, temperature, pressure, and particle size was studied. The results allowed us to conclude that the process is mainly controlled by the equilibrium rather than mass transfer effects. All the experiments were modeled and simulated using a

non-isothermal axially dispersed plug flow model which included all the transport effects. The simulations showed an agreement with the experimental results, which further confirmed the validity of the mathematical model and the assumptions used to describe the experimental data.

2 Materials and methods

The same batch of Ag-ETS-10 extrudates as in the earlier publications on the breakthrough and cycle development studies [10–12] has been used in this study. This batch has been repeatedly used in various experimental campaigns over a period of 6 years including experiments with more than 100 cycles and have shown maximum stability over this period. Physical properties of the sorbent are reported in Table 1. To study the particle size effect on the dynamics of adsorption, these extrudates (d_p = 1.2 mm, L_p = 10 mm) were crushed and sieved to 0.5 mm granules. All gases in this study (99.999% N_2, 99.999% Ar, 99.999% He, 95.0% O_2/5.0% Ar, and 50.0% O_2/50.0% Ar) were obtained from

Praxair Canada Inc. Prior to each set of experiments, Ag-ETS-10 particles were activated for 16 h at 523.15 K under a N_2 environment.

2.1 Isotherm measurements

Low pressure isotherms for N_2, O_2, and Ar at multiple temperatures were obtained using the volumetric method and are reported in Fig. 1. The values of single-site Langmuir model parameters, used to describe the isotherms, are provided in the Supporting Information. High-pressure isotherms of pure N_2, O_2, and Ar on Ag-ETS-10 were measured using a HPVA-100 high pressure volumetric unit from VTI instruments (Hialeah, FL). The measured adsorption isotherms are shown in Fig. 1d. In Ag-ETS-10, the separation mechanism is equilibrium-based and as expected, N_2 shows the strongest adsorption due to its stronger quadrupole moment. We further note that the equilibrium in the adsorption chamber was reached within a few seconds for the experimental points in Fig. 1 which implies a negligible micropore resistance in

Table 1 Parameters used in dynamic column breakthrough simulations

Parameter	Value		Source
Column properties	Column 1	Column 2	
Column length, L [m]	0.32	0.062	Measured
Inner column radius, r_{in} [m]	0.01805	0.0080	Measured
Outer column radius, r_{out} [m]	0.02415	0.0095	Measured
Column void fraction, ϵ	0.32	0.30	Measured
Particle voidage, ϵ_p	0.35	0.35	Assumed
Tortuosity, τ	3	3	Assumed
Properties and constants			
Universal gas constant, R [m^3 Pa mol^{-1} K^{-1}]	8.314		Standard value
Adsorbent particle density, ρ_s [kg m^{-3}]	990		Measured
Column wall density, ρ_w [kg m^{-3}]	7800		Standard value for stainless steel
Specific heat capacity, $C_{p,g}$ [J kg^{-1} K^{-1}]	1041.3 (N_2), 895.63 (O_2) and 521.45 (Ar)		Standard values
Specific heat capacity of adsorbed phase, $C_{p,a}$ [J kg^{-1} K^{-1}]	1041.3 (N_2), 895.63 (O_2) and 521.45 (Ar)		Assumed
Specific heat capacity of adsorbent, $C_{p,s}$ [J kg^{-1} K^{-1}]	715.9		Fitted
Specific heat capacity of column wall, $C_{p,w}$ [J kg^{-1} K^{-1}]	502		Standard value for stainless steel
Fluid viscosity, μ [kg m^{-1} s^{-1}]	1.801×10^{-5} (N_2), 2.095×10^{-5} (O_2), 2.291×10^{-5} (Ar)		Standard values
Molecular diffusivity, D_m [m^2 s^{-1}]	7.2×10^{-5} (N_2), 7.9×10^{-5} (O_2) 7.6×10^{-5} (Ar)		Standard values
Mass transfer coefficient in LDF model, k_i [s^{-1}]	502 (N_2), 553 (O_2), and 546 (Ar)		Calculated
Effective gas thermal conductivity, K_z [J m^{-1} K^{-1} s^{-1}]	0.0903		Assumed
Thermal conductivity of column wall, K_w [J m^{-1} K^{-1} s^{-1}]	16		Standard value for stainless steel
Inside heat transfer coefficient, h_{in} [J m^{-2} K^{-1} s^{-1}]	15.2		Fitted
Outside heat transfer coefficient, h_{out} [J m^{-2} K^{-1} s^{-1}]	1462.1		Fitted
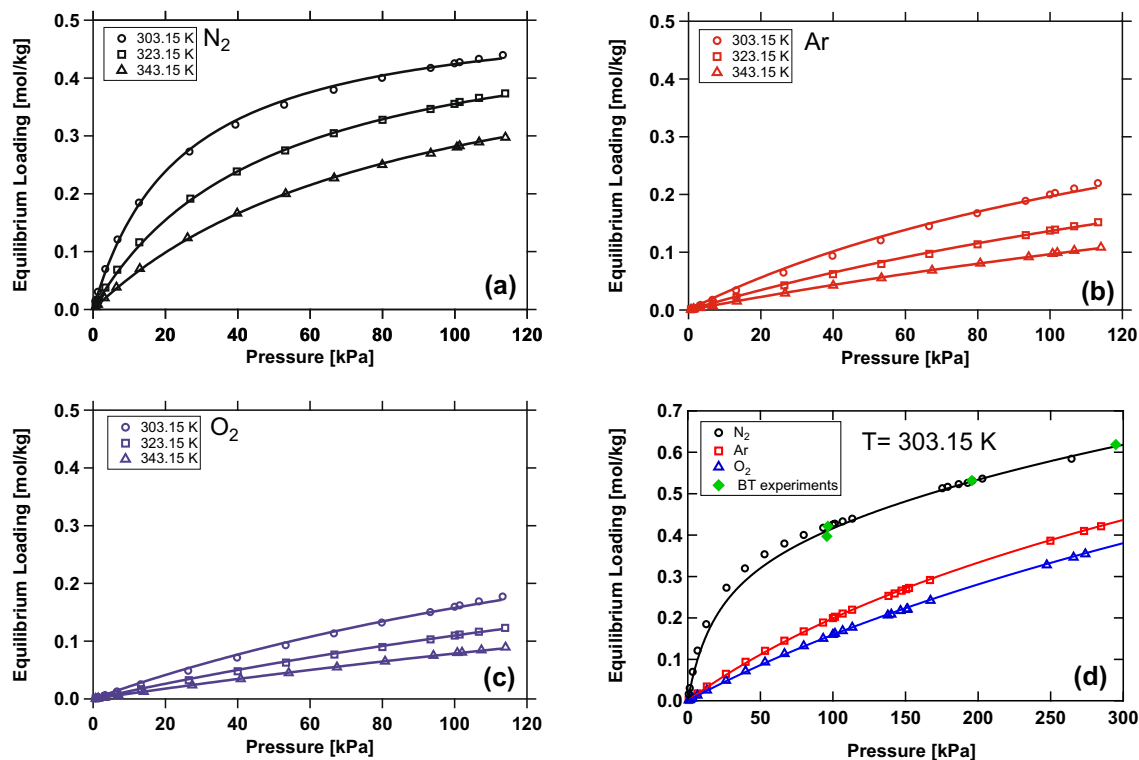
Fig. 1 Single component low pressure (**a**–**c**) and high pressure (**d**) adsorption isotherms of **a** N_2, **b** Ar, and **c** O_2 on Ag-ETS-10 extrudates. Symbols are experimental values while lines are fitted to a Langmuir model. **d** High pressure adsorption isotherms of N_2, Ar, and O_2 on Ag-ETS-10 extrudates at 303.15 K. Symbols are experimental values and lines correspond to dual-site Langmuir model. The green symbols are calculated from mass balance calculations of the breakthrough experiment at 303.15 K [11, 12]

Ag-ETS-10 particles. Dual-site Langmuir adsorption model was used to describe the pure component isotherms:

$$q_i^* = \frac{q_{sb,i}b_ic_i}{1+b_ic_i} + \frac{q_{sd,i}d_ic_i}{1+d_ic_i} \tag{1}$$

where q_i^* is the equilibrium solid phase concentration of component i and c_i represents the gas phase concentration. The solid phase saturation capacities at the two adsorption sites are $q_{sb,i}$ and $q_{sd,i}$ (mol/kg), respectively. Temperature-dependant adsorption equilibrium constants, b_i and d_i, are described by the van't Hoff formulation:

$$b_i = b_{0,i}e^{\frac{-\Delta U_{b,i}}{RT}} \tag{2}$$

$$d_i = d_{0,i}e^{\frac{-\Delta U_{d,i}}{RT}} \tag{3}$$

where $U_{b,i}$ and $U_{d,i}$ are the internal energies of component i for the two adsorption sites. The sets of parameters in Eqs. 1 to 3 were fitted simultaneously to the experimental isotherm points using the nonlinear regression function `nlinfit` in MATLAB. The values of the fitted parameters are reported in Table 2. We note that the binary data has been measured, validated, and described well by the competitive isotherms

Table 2 Fitted dual-site Langmuir adsorption parameters to high-pressure isotherms for N_2, O_2, and Ar on Ag-ETS-10 [11]

Parameter	N_2	Ar	O_2
$b_{0,i}$ [m³ mol⁻¹]	3.32×10^{-6}	6.87×10^{-6}	8.55×10^{-6}
$d_{0,i}$ [m³ mol⁻¹]	2.42×10^{-4}	1.18×10^{-5}	1.42×10^{-5}
$q_{sb,i}$ [mol kg⁻¹]	1.06	0.46	0.33
$q_{sd,i}$ [mol kg⁻¹]	0.37	1.71	1.69
$-\Delta U_{b,i}$ [kJ mol⁻¹]	17.06	18.41	17.22
$-\Delta U_{d,i}$ [kJ mol⁻¹]	15.71	11.25	11.26

[12]. The parameters fitted to the low-pressure isotherms were used to simulate the breakthrough curves obtained to study the effect of temperature and flow rate while high-pressure isotherms have been used to model the curves to explore the effect of pressure.

2.2 Dynamic column breakthrough experiments

A systematic approach was taken to eliminate or to confirm presence of various physical mechanisms. To this aim, the effect of four physical and operating parameters, namely particle size, flow rate, temperature, and pressure was explored.

In each phase of the study, one parameter was changed while the others were kept constant. A fully-automated experimental apparatus was used to conduct the breakthrough experiments. A schematic of the DCB apparatus used in this study is depicted in the Supporting Information. We note that columns of two different sizes have been used in this study. Column 1 refers to the larger column that was 32 cm long and 3.7 cm in diameter while column 2 was 6.2 cm long and had an inner diameter of 1.6 cm. Column 1 was used to investigate the effects of temperature and flow rate while column 2 was used to explore the effects of particle size and pressure. A summary of the experimental campaign is reported in Table 3.

Two mass-flow controllers and a mass flow meter (Parker/Porter, Hatfield, PA, USA) were used to control and measure the flow of the streams entering and leaving the column, respectively. Inlet and differential pressures across the column were measured using two pressure transducers (GE Druck, Billerica, MA, USA). To achieve higher pressure values than ambient pressures, a back-pressure regulator (Swagelok, Solon, OH, USA) was positioned at the exit. Two thermocouples (Omega Engineering, Stamford, CT, USA), located at 8 and 24 cm from the inlet of Column 1, were used to monitor the internal temperature curves. Experimental temperature was controlled by means of a circulation thermal water bath (PolyScience, Niles, IL, USA) and the outlet gas composition was measured with a mass spectrometer (Pfeiffer Vacuum OmniStar GSD 320, Asslar, Germany). All the operating parameters were recorded and controlled using a LabVIEW-based data acquisition system. A typical breakthrough experiment consisted of (i) an initial saturation of the bed with helium, (ii) adsorption with the test gas, (iii) and desorption with helium. The mass flow controllers, mass flow meter, and the mass spectrometer were all calibrated prior to running experiments in accordance with the required experimental operating conditions.

2.3 Modelling

A generic one-dimensional, axially-dispersed plug flow model, was used to simulate the adsorption and desorption breakthrough curves in this study. Contributions from convection, axial dispersion, adsorption of the gas phase, heat transfer across the column and the wall, and pressure drop are included in this model. Axial dispersion coefficient was described by the following equation [18]:

$$D_L = 0.7D_m + 0.5vd_p \tag{4}$$

where D_m and d_p are the molecular diffusion and particle diameter, respectively, and v is the interstitial velocity. D_m was estimated using Chapman–Enskog formulation. Mass transfer in the solid phase is described using linear driving force (LDF) model:

$$\frac{\partial q_i}{\partial t} = k_i\left(q_i^* - q_i\right) \tag{5}$$

where k_i is the lumped mass transfer coefficient and q_i^* is the solid phase equilibrium capacity of component i. An instantaneous thermal equilibrium is assumed between the solid and the gas phase and the previously fitted heat transfer coefficients in our earlier campaign [12] were used to describe the experimental breakthrough curves in a predictive manner. Mass, momentum, and energy balances across the column were discretized in space based on the principles of the finite volume technique [19] and solved in time using MATLAB's `ode15s` solver. The column is assumed to be initially at the experimental temperature set by the thermal water bath and saturated with helium and feed gas during the adsorption and desorption experiments, respectively. Danckwert's boundary conditions for a dispersed plug flow system are applied to the component mass and column energy balances. Wall temperatures at $z = 0$ and $z = L$ are assumed to be equal to the temperature of the surrounding water bath. Boundary conditions of the overall mass balance were defined by the experimental conditions, i.e. the velocity of the feed gas entering the column at $z = 0$ and the pressure controlled by the regulator at $z = L$. Table 4 summarizes all the equations used in the model.

2.4 Mass balance calculations

The equilibrium amount adsorbed on the solid phase at steady-state conditions in any DCB experiments can be estimated from a material balance around the adsorption column:

Table 3 Summary of the experimental parametric study on Ag-ETS-10 particles

Variable parameter	Type	Gas	Column	Purpose
Particle size	Ads	N$_2$	2	Eliminate/confirm macropore
Flow rate	Ads/Des	O$_2$, Ar	1	Confirm axial-dispersion, Eliminate film resistance
Temperature	Ads/Des	N$_2$,O$_2$, Ar	1	Confirm self-sharpening, eliminate/confirm mass transfer resistance
Pressure	Ads	N$_2$	2	Confirm self-sharpening, eliminate/confirm mass transfer resistance

$$\int_0^t \left(\frac{F_{in}P_{in}y_{in}}{RT_{in}} \right) dt - \int_0^t \left(\frac{F_{out}P_{out}y_{out}}{RT_{out}} \right) dt = M_{ads}q_i^* + \frac{(V_b\epsilon + V_d)P_{avg}y_{in}}{RT} \tag{6}$$

The left hand side of the above equation represents the difference between the amount of component i entering and leaving the column for the duration of experiment. F, P, y, and T in these two terms are the corresponding experimental values recorded for the flow rate, pressure, composition, and temperature, respectively. On the RHS of the equation, the first term represents the amount adsorbed in the solid phase while the second terms is the accumulated adsorbate in the fluid phase and dead volume of the experimental rig. M_{ads} is the amount of adsorbent packed inside the column, V_b is the bed volume, ϵ is the bed porosity, P_{avg} is the arithmetic mean of experimental inlet and outlet pressures, and V_d is the dead volume which was found to be 15 cc. Since this was considered to be small compared to the capacity of the column, a point-by-point correction was performed to adjust the breakthrough curves [20]. Hence, Eq. 6 can be rearranged to calculate q_i^*, the amount of component i adsorbed per unit mass of the solid phase for dynamic breakthrough experiment.

3 Results and discussion

Four sets of experiments were conducted to study the effect of multiple parameters on the breakthrough curves, namely the flow rate, temperature, pressure, and the adsorbent particle size. The same batch of Ag-ETS-10 was consistently used for all the experiments. In each of the sections below, only one parameter was changed while the other operating conditions were fixed. The objective of these experiments were to identify the importance of mass transfer effects, axial-dispersion within the column, and thermodynamics of adsorption in determining dynamics of this separation.

3.1 Sensitivity analysis of mass transfer coefficient

It has been reported [17] that for systems with fast mass transfer nature, similar to the one in this study, estimation and experimental measurement of mass transfer coefficient, k_i, from DCB experiments could be potentially inaccurate. We have further investigated this by varying k_i in LDF formulation over three orders of magnitude as shown in Fig. 2 where Ar breakthrough curves at 313.15 K are simulated with various values of k_i, viz. 5.8, 58, and 580 s^{-1}. The column was initially saturated with pure helium and Ar was then introduced to the bed at constant flow rate of 150 ccm. Symbols represent the experimental composition curve measured at the outlet and the lines correspond to the simulations each using a single value of k_i. The comparison of the simulated curves clearly indicates that the predicted
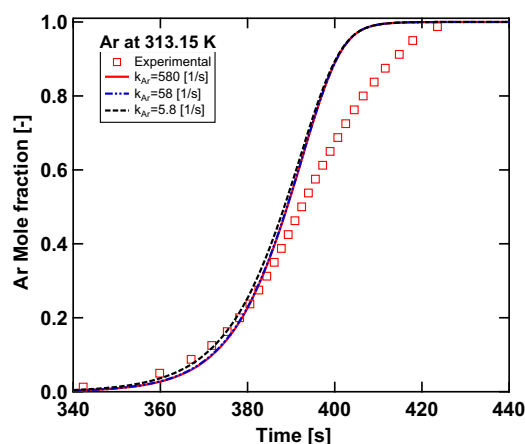
Fig. 2 Sensitivity analysis of the effect of mass transfer coefficient, k_i, on simulated adsorption breakthrough curve of Ar. Experimental conditions: P_{avg}=95 kPa, T_{bath}=313.15 K, F_{in}=150 ccm

breakthrough curves are indistinguishable and all values of k_i can be used for describing the mass transfer. Hence, we use the values of k_i reported in Table 1, sufficient to describe our previous cycle development experiments [10, 11], for all further simulations. We note that the axis in Fig. 2 is zoomed for better visualization and the difference between the simulated and experimental breakthrough curve is $\approx 5s$ compared to the breakthrough time of $\approx 400s$.
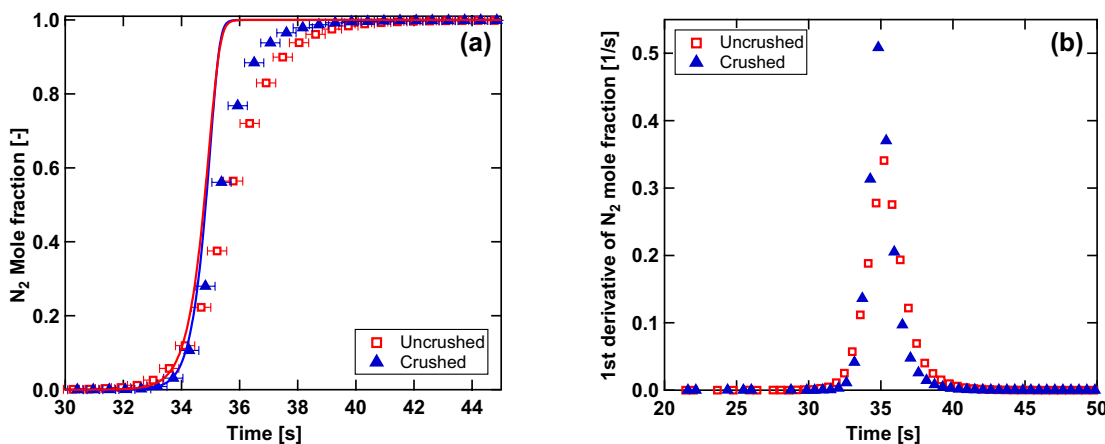
3.2 Effect of particle size

The first group of experiments performed as a part of this study was to investigate the effect of particle size on the breakthrough curves. The un-crushed cylindrical extrudates were initially packed in column 2. The bed was flushed with pure helium and the outlet composition was monitored to ensure achieving a complete regeneration prior to introducing N_2 at 150 ccm. Once completed, the same particles were crushed and sieved to make granules with average diameter of 0.5 mm and the same column was packed with the same mass of Ag-ETS-10 granules as in the case of cylindrical extrudates. The bed was then regenerated and N_2 breakthrough curve at 303.15 K, 95 kPa, and 150 ccm feed flow rate was obtained. Figure 3a shows the breakthrough curves for both the crushed (blue) and un-crushed (red) Ag-ETS-10 particles and the corresponding first derivatives (slope) of the composition curves are also shown in Fig. 3b. The first derivative of the curves at time step i was calculated as:

$$\left(\frac{\Delta y}{\Delta t} \right)_i = \frac{y_{i+1} - y_i}{t_{i+1} - t_i} \tag{7}$$

Table 4 Equations for modeling adsorption column dynamics

| Overall mass balance	$\frac{1}{P}\frac{\partial P}{\partial t} - \frac{1}{T}\frac{\partial T}{\partial t} = -\frac{T}{P}\frac{\partial}{\partial z}\left(\frac{P}{T}v\right) - \frac{RT}{P}\frac{1-\epsilon}{\epsilon}\sum_{i=1}^{n_{comp}}\frac{\partial q_i}{\partial t}$
Component mass balance	$\frac{\partial y_i}{\partial t} + \frac{y_i}{P}\frac{\partial P}{\partial t} - \frac{y_i}{T}\frac{\partial T}{\partial t} = \frac{T}{P}D_L\frac{\partial}{\partial z}\left(\frac{P}{T}\frac{\partial y_i}{\partial z}\right) - \frac{T}{P}\frac{\partial}{\partial z}\left(\frac{y_i P}{T}v\right) - \frac{RT}{P}\frac{1-\epsilon}{\epsilon}\frac{\partial q_i}{\partial t}$
Solid phase mass balance	$\frac{\partial q_i}{\partial t} = k_i\left(q_i^* - q_i\right)$
Pressure drop	$-\frac{\partial P}{\partial z} = \frac{150}{4}\frac{1}{r_p^2}\left(\frac{1-\epsilon}{\epsilon}\right)^2\mu v$
Column energy balance	$\left[\frac{1-\epsilon}{\epsilon}\left(\rho_s C_{p,s} + C_{p,a}\sum_{i=1}^{n_{comp}}q_i\right)\right]\frac{\partial T}{\partial t} = \frac{K_z}{\epsilon}\frac{\partial^2 T}{\partial^2 z} - \frac{C_{p,g}}{R}\frac{\partial}{\partial z}(vP) - \frac{C_{p,g}}{R}\frac{\partial P}{\partial t} - \frac{1-\epsilon}{\epsilon}C_{p,a}T\sum_{i=1}^{n_{comp}}\frac{\partial q_i}{\partial t}$ $+\frac{1-\epsilon}{\epsilon}\sum_{i=1}^{n_{comp}}\left((-\Delta H_i)\frac{\partial q_i}{\partial t}\right) - \frac{2h_{in}}{\epsilon r_{in}}(T - T_w)$
Wall energy balance	$\rho_w C_{p,w}\frac{\partial T_w}{\partial t} = K_w\frac{\partial^2 T_w}{\partial^2 z} + \frac{2r_{in}h_{in}}{r_{out}^2 - r_{in}^2}(T - T_w) - \frac{2r_{out}h_{out}}{r_{out}^2 - r_{in}^2}(T_w - T_a)$

Fig. 3 Effect of particle size on the adsorption breakthrough curves for N_2. **a** composition curve at the column outlet; **b** corresponding 1st derivative of the composition curve. Symbols and lines correspond to experimental and simulation data, respectively. Error bars in (**a**) represent accuracy of breakthrough curve measurements in time calculated based on the accuracy of flow measurements (0.5% reading plus 0.1% full scale). Experimental conditions: P_{avg}=95 kPa, T_{bath}=303.15 K, F_{in}=150 ccm

Figure 3a indicates that there is almost no change in the adsorption capacity of Ag-ETS-10 particles after the crushing since the breakthrough curves lie exactly on top of each other. As shown in Fig. 3b, a marginally sharper breakthrough curve is obtained for the crushed granules compared the un-crushed ones. We suspect that this could be due to the smaller axial dispersion in the granules as compared to the cylindrical extrudates, although this difference is too small to have a major effect on the performance of the process. We emphasize that the minimal difference between the curves of the crushed and un-crushed particles confirms the fast mass transfer nature of N_2 within the macropores of Ag-ETS-10 particles. The solid lines in Fig. 3a are the predictions from the model using macropore resistance formulation to predict the mass transfer coefficient in linear driving force model, k_i. The discrepancy observed between the model prediction and the experimental breakthrough curves might be due to the wall effects resulting from the smaller ratio of bed diameter to the particle size in column 2. We note that the error bars in the same figure represent the accuracy of the experimental measurements which further verifies minimal effect of particle size on the breakthrough curve. In fact, these experiments demonstrate that there is minimal resistance in the macropores.
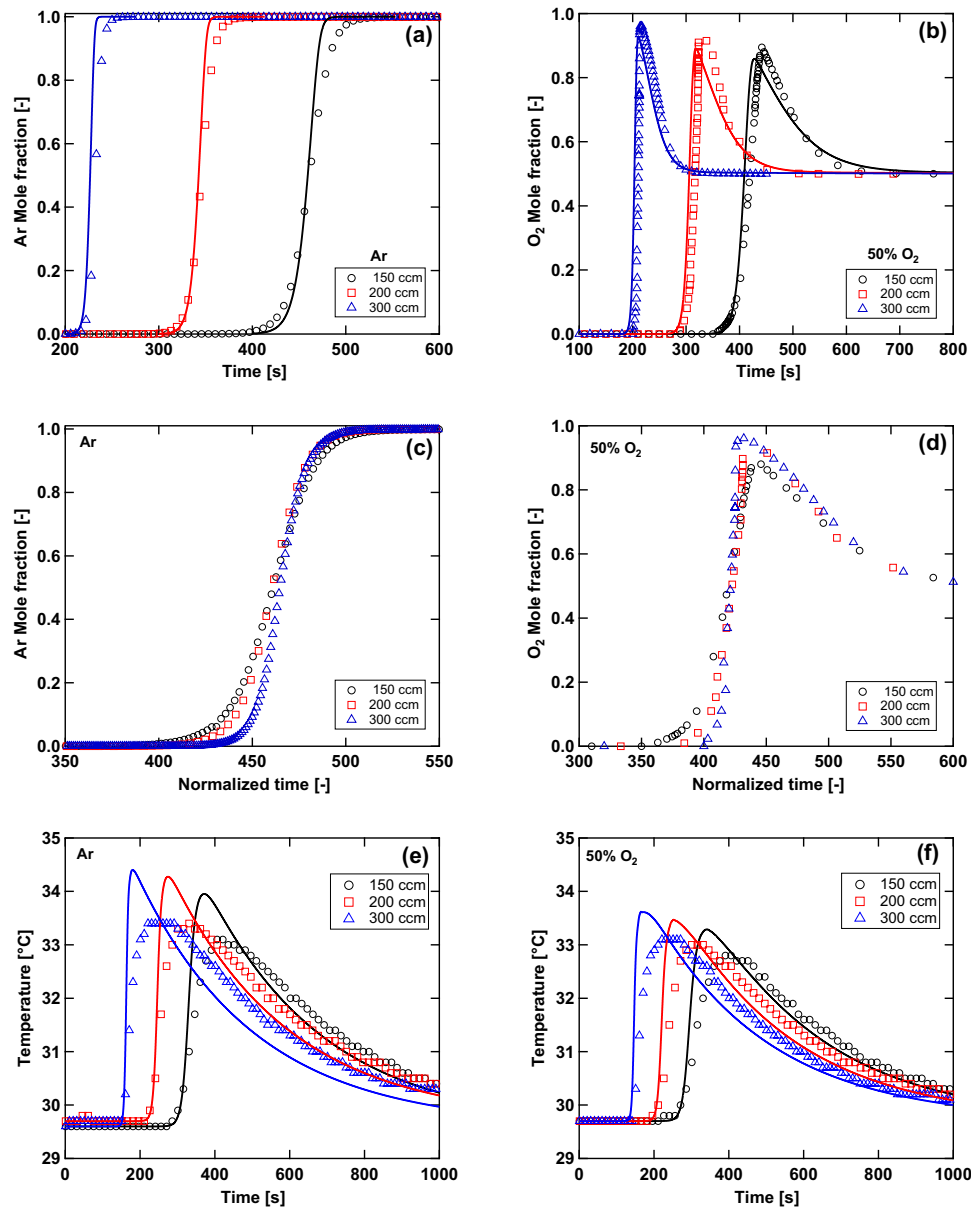
Fig. 4 Effect of inlet flow rate on the adsorption breakthrough curves for Ar and 50.0% O_2/50.0% Ar. **a** and **b** Composition curves at the column outlet; **c** and **d** experimental composition at the column outlet against normalized time; **e** and **f** temperature curves measured by thermocouple 1 (T_1). Symbols and lines correspond to experimental and simulation data, respectively. Experimental conditions: P_{avg}=95 kPa, T_{bath}=303.15 K

3.3 Effect of flow rate

We present in this section the effect of three different flow rates on the adsorption breakthrough and desorption curves of pure Ar and 50% O_2/ 50% Ar mixture. Column 1 was initially purged with helium and the test gas was introduced to the column at flow rates of 150 ccm, 200 ccm, and 300 ccm. Figure 4a and c show the corresponding breakthrough curves against absolute and normalized time for pure Ar experiments, respectively. The temperature curves for the thermocouple located at 8 cm from the column inlet is also shown in Fig. 4e.

Figure 4c indicates the composition front is sharper for the higher flow rates which is possibly due to the larger Peclet numbers for higher flow rates (i.e. higher velocities). Peclet number is defined as:

$$Pe = \frac{v d_p}{D_L} \tag{8}$$

where D_L is the axial dispersion coefficient and is described by Eq. 4. Peclet number can be also defined as the product of Reynolds and Schmidt numbers:

$$Pe = ReSc \tag{9}$$

We note that the Reynolds number for the experiments conducted in this study was in the range of 0.15–0.3 and Schmidt number was calculated to be ≈ 0.2, hence, resulting in Peclet numbers between 0.03 to 0.06 which confirms the system is far from the convection-dominated regime [18]. This implies that the first term on the right-hand side in Eq. 4 is dominating over the second term and therefore, according to Eqs. 4 and 8, Peclet number, i.e. ratio of convective to dispersive transport, increases with increasing velocity. This implies a relatively sharper breakthrough curves at higher flow rates similar to what is observed in Fig. 4c. Macro/micropore diffusion resistances are not affected by the change in velocity of the feed if all other operating conditions are kept unchanged. The only other mass transfer resistance affected by the velocity of the fluid is the external film resistance, k_f, defined as [18]:

$$k_f = \frac{ShD_m}{2r_P} \tag{10}$$

where D_m and Sh are the molecular diffusion of the fluid and the Sherwood number, respectively. Sherwood number is calculated using the Wakao and Funazkri correlation [21]:

$$Sh = 2.0 + 1.1Sc^{1/3}Re^{0.6} \tag{11}$$

where Sc and Re are the Schmidt and Reynolds numbers, respectively. The former is independent of the fluid velocity while the latter increases at higher velocities. Therefore, according to Eqs. 10 and 11, once the flow rates of the fluid increases, k_f has a larger magnitude (less resistance) which results in sharper breakthrough curves. However, for the range of velocities used in these experiments, Sherwood number, defined as the ratio of the convective mass transport to the rate of diffusive mass transport, was around the lower limit of 2.0 estimated by Eq. 11. Hence, the change in the steepness of the breakthrough curves is likely from the change in the Peclet number rather than external film resistance. This observation was further verified by comparing the magnitude of dispersion and film resistance effects through parameter δ [18]:
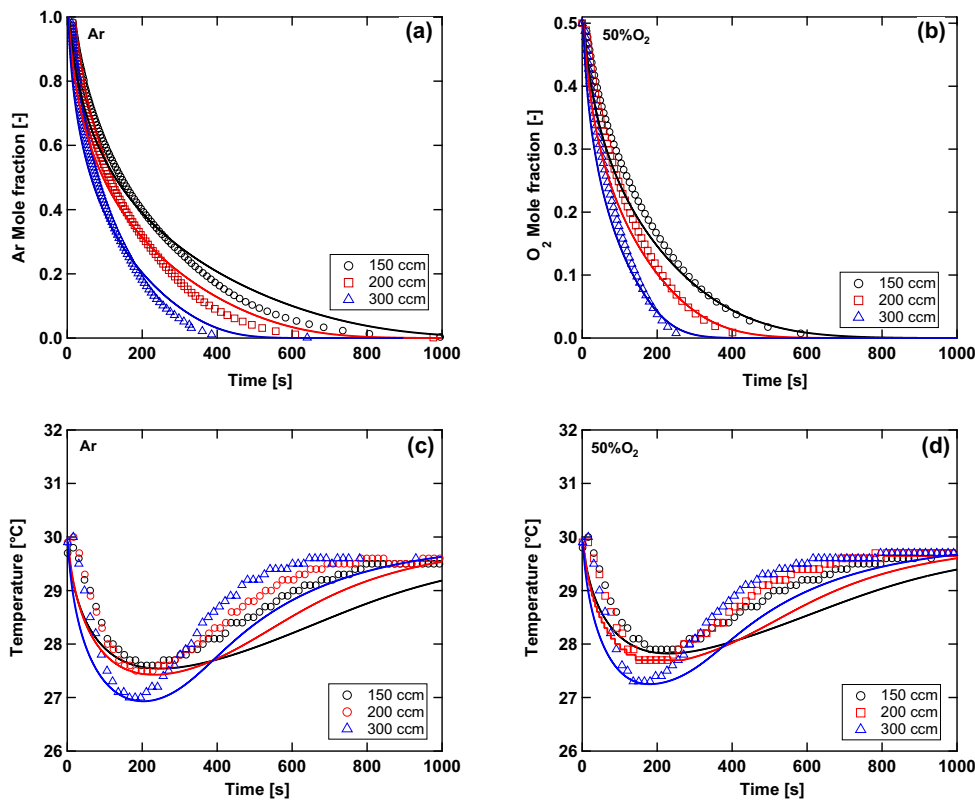

Fig. 5 Effect of inlet flow rate on the desorption breakthrough curves for Ar and 50.0% O_2/50.0% Ar. **a** and **b** show composition curves at the column outlet; **c** and **d** show corresponding temperature curves measured by thermocouple 1 (T_1). Symbols and lines correspond to experimental and simulation data, respectively. Experimental conditions: P_{avg}=95 kPa, T_{bath}=303.15 K

$$\delta = \left(\frac{1 - \epsilon}{\epsilon} \right) \left(\frac{3k_f}{R_p} \right) \left(\frac{D_L}{v^2} \right) \quad (12)$$

δ in the case of these experiments, is in order of 500–2000 which essentially means axial dispersion had significantly larger contribution compared to the external film resistance [18]. We further note that the model is able to predict the experimental curves for all the three flow rates in a satisfactory manner.

On panels (b), (d), and (f) of Fig. 4 are shown the effect of flow rate for a 50.0% O_2/50.0% Ar mixture with the same range of inlet flow rates. Same effect as in the case of pure Ar experiments are seen for 50.0% O_2/50.0% Ar feed, i.e., sharper fronts are observed at higher flow rates. It is worth noting that higher purities of O_2 at the outlet is detected when the feed flow rate is larger. This effect is well captured by the model and is possibly due to the sharper O_2 front traveling through the column at higher inlet velocity. We further note the larger

temperature rise in the thermocouple located at 8 cm from the inlet at higher velocities as shown in Fig. 4e and f which is possibly due to the larger contribution of the convective heat transfer at higher flow rates. It is worth noting that the temperature curves corresponding to pure Ar show a slightly higher increase compared to the 50/50 mixture due to its stronger adsorption affinity than O_2 which further verifies the accuracy of the DCB experiments. Figure 5 shows desorption curves of the same set of experiment for pure Ar in panel (a) and 50.0% O_2/50.0% Ar mixture in panel (b). Similar to adsorption experiments, the steeper decrease in the composition is attributed to larger Peclet numbers at higher flow rates and pure argon shows a relatively longer desorption period inline with its higher adsorbed amount on Ag-ETS-10 compared to O_2 as shown in Fig. 1d. The temperature curves for the desorption experiments are shown in Fig. 5c and d which again shows both a larger temperature drop and a faster recovery back to the equilibrium temperature at higher velocities due to stronger
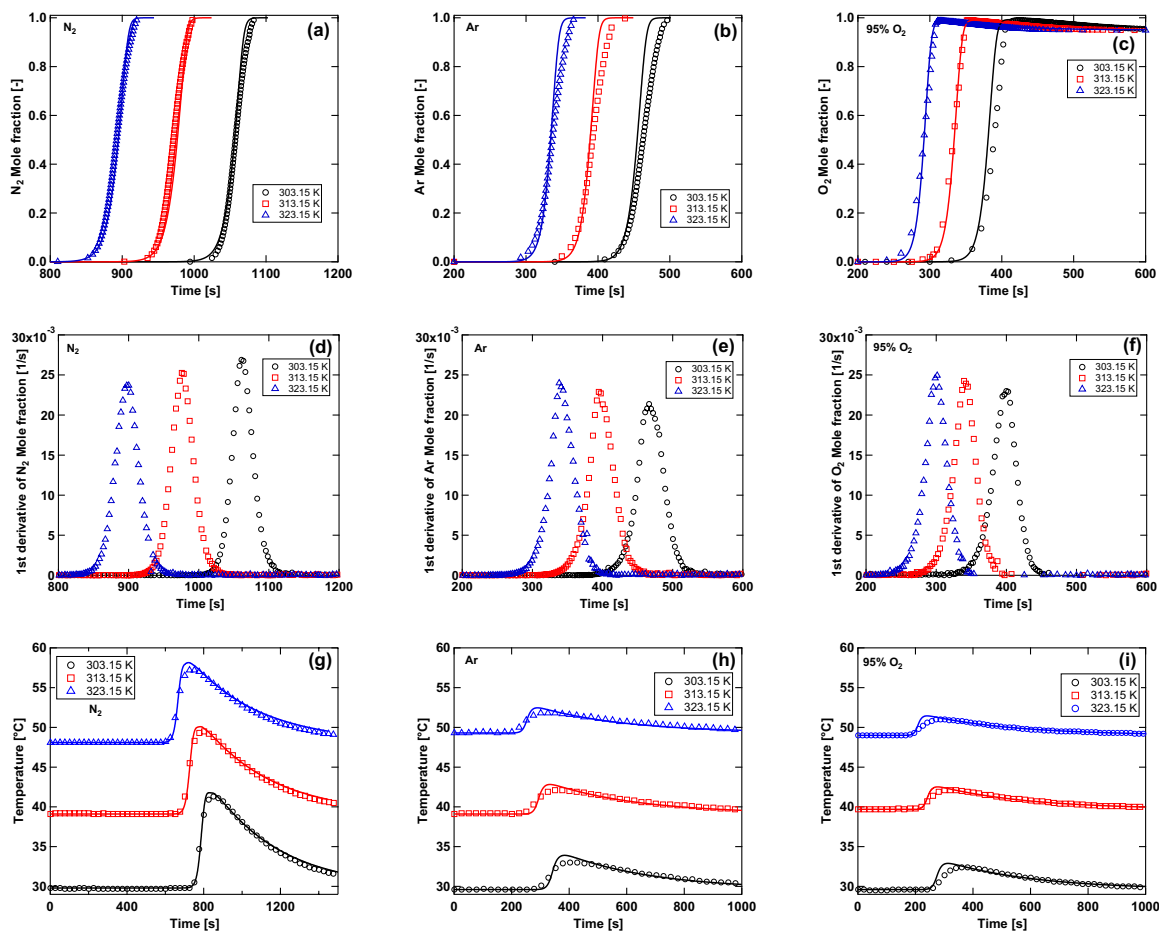
Fig. 6 Effect of temperature on the adsorption breakthrough curves for N_2, Ar and 95.0% O_2/5.0% Ar. **a–c** Composition curves at the column outlet; **d–f** corresponding 1st derivative of the composition curves; **g–i** corresponding te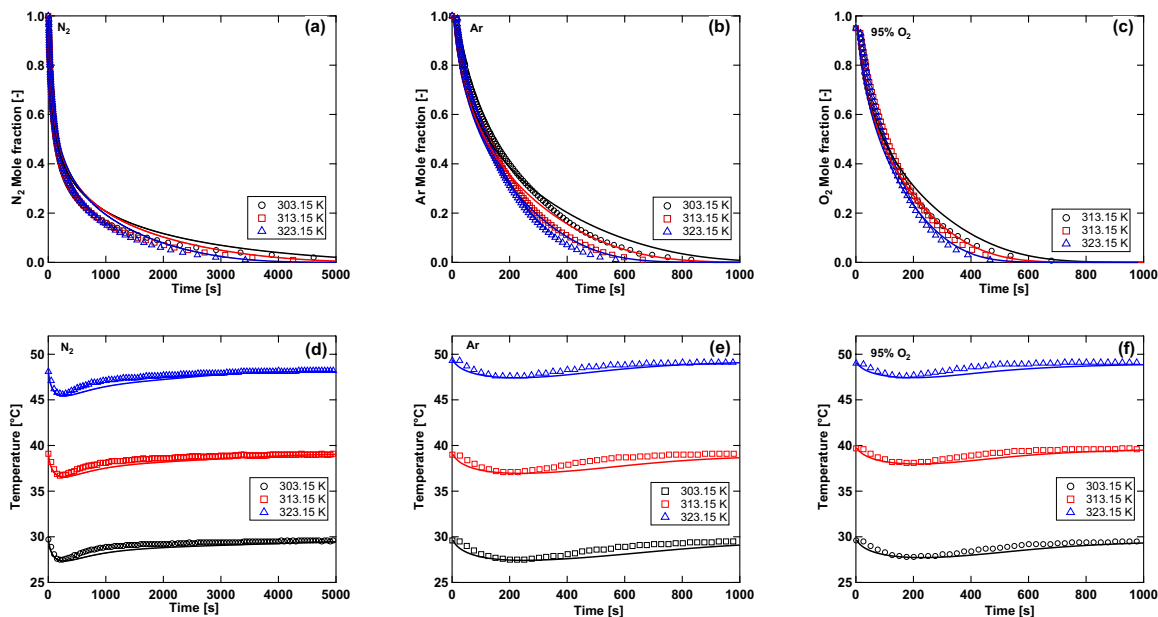mperature curves measured by thermo-couple 1 (T_1). Symbols and lines correspond to experimental and simulation data, respectively. Experimental conditions: P_{avg}=95 kPa, F_{in}=150 ccm

convective heat transfer effects. This results in an overlap in the experimental temperature curves as can be seen in Fig. 5(c) and (d) and is also predicted by the model. We emphasize that the model is used in a fully predictive manner and the ability to capture effects such as this or the overshoots in O_2 breakthrough curves at multiple flow rates shown in Fig 4b, further verifies its potential to precisely describe high-purity O_2 separation adsorption cycles as reported in our earlier publication [10]. Further, the result presented in this section verifies the important role of axial-dispersion in designing rapid cycles aiming at high-purity products.

3.4 Effect of temperature

The third set of experiments were conducted to study the effect of temperature on the adsorption breakthrough and desorption curves of pure N_2, Ar, and 95.0% O_2/5.0% Ar. Adsorption breakthrough experiments were conducted at 303.15 K, 313.15 K, and 323.15 K. The temperature of the experiments were controlled using an automated water circulation bath. The inlet flow rate for all these experiments was kept constant at 150 ccm. The column dimensions used in this section were similar to the previous section and are summarized in Table 1 (column 1). Figure 6a to c show the composition of the stream leaving the adsorption column and the corresponding first derivatives are shown in Fig. 6d to f. The experimental temperature curves for the thermocouple located at 8 cm from the column inlet are shown in Fig. 6g to i. As it can be observed in these figures, N_2 breakthrough

curves are sharper at lower temperatures whereas the opposite trend is observed for Ar and O_2 (i.e. sharper fronts at higher temperatures). The trend observed for N_2 curves is a thermodynamic effect, i.e. sharper breakthrough at lower temperatures due to the increase in the non-linearity of the N_2 isotherms and therefore, stronger self-sharpening effect as compared to the relatively linear ones for Ar and O_2. If the mass transfer were the limiting phenomena, similar trends should have been observed for all the three gases by varying the temperature since the diffusion rate increases at higher temperatures. The opposite trend observed for O_2 and Ar might arise from multiple effects such as the larger diffusion coefficient at higher temperatures, stronger heat effects at elevated temperatures, or relatively linear isotherms of Ar and O_2 as compared to the non-linear ones for N_2. To make a conclusion, one needs to simultaneously compare the results on the effect of temperature for both adsorption and desorption experiments for all three components. Figure 7 shows similar results for the effect of temperature on the desorption curves for the same set of experiments. The striking feature of the results shown in this figure is that N_2 desorption composition curves at all the temperatures initially overlap as shown in panel (a) and start to spread out at around composition value of 0.2. However, for Ar and O_2, the curves at higher temperatures decrease at a faster rate compared to the ones at lower temperatures as soon as the desorption step starts. This effect is again attributed to the non-linear nature of N_2 isotherms, i.e. initially the leading state [22] travels with roughly similar speed at different temperatures owing to the similar slope of

Fig. 7 Effect of temperature on the desorption breakthrough curves for N_2, Ar and 95.0% O_2/5.0% Ar. **a**–**c** Composition curves at the column outlet; **d**–**f** corresponding temperature curves measured by thermocouple 1 (T_1). Symbols and lines correspond to experimental and simulation data, respectively. Experimental conditions: P_{avg}=95 kPa, F_{in}=150 ccm

the tangent to the N_2 isotherms at 303.15 K, 313.15 K, and 323.15 K and 95 kPa, whereas the relatively linear isotherms of Ar and O_2 result in different desorption rates at different initial states (i.e. the saturated column at 95 kPa and the three different experimental temperatures). These observations clearly indicate that the shape of the breakthrough curves in this set of experiments is governed by the thermodynamics of the process rather than mass transfer effect. We also note that the model can closely describe the experimental composition and temperature curves as shown by the solid lines in Figs. 6 and 7.

3.5 Effect of pressure

We present in this section the effect of operating pressure on the breakthrough curves of the same batch of Ag-ETS-10 extrudates (1.2 mm diameter) packed into column 2. Nitrogen breakthrough curves were obtained at 96.5 kPa, 195.7 kPa, and 294.9 kPa while keeping the temperature and the flow rate constant at 303.15 K and 150 ccm, respectively. The amount of gas adsorbed in these three breakthrough runs were calculated from the mass balance around the column and are shown as green symbols in Fig. 1. We emphasize on the good agreement with the independent volumetry data which further verifies the accuracy of the breakthrough experiments. Figure 8a and b present the corresponding breakthrough curves at three different pressures and the first derivatives of the composition curves, respectively. As expected from the equilibrium theory, for the case of systems following Type-I isotherms, the composition front at higher pressures propagates faster along the column compared to lower pressures resulting in shorter breakthrough times [23]. We note that N_2 breakthrough curves are relatively sharper at higher pressure as shown in Fig. 8b. In accordance to Eq. 4, since D_m is smaller at higher pressures, D_L also decreases (i.e. larger Peclet numbers) and could potentially make the composition fronts steeper, in addition to the equilibrium effects. However, based on the observations in section 3.3, self-sharpening effect and thermodynamics of the process

seem to dominate these experiments. The minor discrepancies between the model predictions and the experimental data in Fig. 8a is possibly due to the wall effects [24] resulting from the smaller ratio of bed diameter to the particle size compared to the previous section in which the bed with a larger diameter was used. Further, it is also worth pointing out that systems controlled by molecular diffusion in the macropores will show an increased spread at higher pressures as D_m reduces with increasing pressure. The absence of such effects further confirm that equilibrium effects dominate the dynamics compared to the mass transfer effects. We further note that including Ar and O_2 in studying the effects of pressure and particle size would have assisted to rule out mass transfer resistance with more confidence. However, as shown in Table 3, these two effects were studied using the smaller column due to the limited amount of crushed granules available. Since both Ar and O_2 are weakly adsorbed on Ag-ETS-10, running experiments with these gases in the smaller column would have resulted in very short breakthrough times. This would have introduced a lot of uncertainty in the analysis and was therefore not considered. Hence, N_2 was chosen deliberately to study the effect of pressure and particle size due to its stronger adsorption and larger molecule size as compared to O_2 and Ar.

4 Conclusions

In this work, the effects of flow rate, temperature, pressure, and particle size on the breakthrough curves of N_2, O_2, and Ar and their mixtures on Ag-ETS-10 extrudates and granules were investigated using a laboratory scale dynamic column breakthrough apparatus. A systematic parametric study was conducted to identify the governing physical mechanisms. N_2 composition curves on two columns filled with Ag-ETS-10 extrudates and granules with two different sizes were obtained. Although a minor effect of particle size was observed, the result suggested that mass transfer through Ag-ETS-10 particle is less likely to dominate the separation

Fig. 8 Effect of pressure on the adsorption breakthrough curves for N_2. **a** Composition curve at the column outlet; **b** corresponding 1st derivative of the composition curve. Symbols and lines correspond to experimental and simulation data, respectively. Experimental conditions: T_{bath} = 303.15 K, F_{in} = 150 ccm
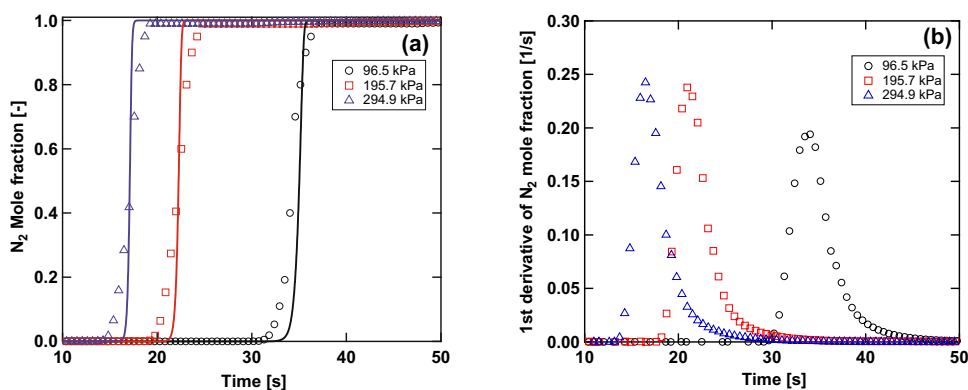
process. It was concluded that the sharper curves obtained at higher inlet velocities were likely due to the change in the dynamics of the system (i.e. larger Peclet numbers) rather than external film resistance. The effect of temperature on the breakthrough curves was also studied and the result indicated that the shape of the composition curves were governed by the thermodynamics of the adsorption rather than mass transfer effects. The same conclusion was reached by exploring the effect of pressure on N_2 breakthrough curves which implied self-sharpening effects at higher pressures. Finite volume technique was used to discretize the partial differential equations to model the experimental data. This model was able to predict the experimental composition and temperature curves of the adsorption and desorption experiments. We emphasize that the results in this study further verify the potential of Ag-ETS-10 for high-purity O_2 production at larger scales using RPSA cycles with almost negligible mass transfer resistance. However, we note that understanding the behaviour of Ag-ETS-10 under RPSA conditions using systems such as frequency response is essential.

Compliance with ethical standards

Conflict of interest The authors declare the following competing financial interest(s): S.M.K. has a financial interest in ExtraordinaryAdsorbents, Edmonton, which has commercialized Ag-ETS-10.

References

1. Ackley, M.W.: Medical oxygen concentrators: a review of progress in air separation technology. Adsorption **25**(8), 1437–1474 (2019)
2. Rao, V.R., Farooq, S.: Experimental study of a pulsed-pressure-swing-adsorption process with very small 5A zeolite particles for oxygen enrichment. Ind. Eng. Chem. Res. **53**(33), 13157–13170 (2014)
3. Chai, S.W., Kothare, M.V., Sircar, S.: Rapid pressure swing adsorption for reduction of bed size factor of a medical oxygen concentrator. Ind. Eng. Chem. Res. **50**(14), 8703–8710 (2011)
4. Chai, S.W., Kothare, M.V., Sircar, S.: Numerical study of nitrogen desorption by rapid oxygen purge for a medical oxygen concentrator. Adsorption **18**(2), 87–102 (2012)
5. Rao, V.R., Kothare, M.V., Sircar, S.: Novel design and performance of a medical oxygen concentrator using a rapid pressure swing adsorption concept. AIChE J. **60**(9), 3330–3335 (2014)
6. Wu, C.-W., Vemula, R.R., Kothare, M.V., Sircar, S.: Experimental study of a novel rapid pressure-swing adsorption based medical oxygen concentrator: effect of the adsorbent selectivity of N_2 over O_2. Ind. Eng. Chem. Res. **55**(16), 4676–4681 (2016)
7. Vemula, R.R., Kothare, M.V., Sircar, S.: Performance of a medical oxygen concentrator using rapid pressure swing adsorption process: effect of feed air pressure. AIChE J. **62**(4), 1212–1215 (2016)
8. Ferreira, D., Magalhães, R., Bessa, J., Taveira, P., Sousa, J., Whitley, R.D., Mendes, A.: Study of AgLiLSX for single-stage high-purity oxygen production. Ind. Eng. Chem. Res. **53**(40), 15508–15516 (2014)
9. Kumar, R.: Vacuum swing adsorption process for oxygen production—a historical perspective. Sep. Sci. Technol. **31**(7), 877–893 (1996)
10. Hejazi, S.A.H., Perez, L.E., Pai, K.N., Rajendran, A., Kuznicki, S.M.: Single- and dual-stage high-purity oxygen production using silver-exchanged titanosilicates (Ag-ETS-10). Ind. Eng. Chem. Res. **57**(27), 8997–9008 (2018)
11. Hejazi, S.A.H., Perez, L.E., Rajendran, A., Kuznicki, S.: Cycle development and process optimization of high-purity oxygen production using silver-exchanged titanosilicates. Ind. Eng. Chem. Res. **56**(19), 5679–5691 (2017)
12. Hejazi, S.A.H., Rajendran, A., Sawada, J., Kuznicki, S.: Dynamic column breakthrough and process studies of high-purity oxygen production using silver-exchanged titanosilicates. Ind. Eng. Chem. Res. **55**(20), 5993–6005 (2016)
13. Vemula, R.R., Kothare, M.V., Sircar, S.: Lumped heat and mass transfer coefficient for simulation of a pressure swing adsorption process. Sep. Sci. Technol. **52**(1), 35–41 (2017)
14. Knox, J.C., Ebner, A.D., LeVan, M.D., Coker, R.F., Ritter, J.A.: Limitations of breakthrough curve analysis in fixed-bed adsorption. Ind. Eng. Chem. Res. **55**(16), 4734–4748 (2016)
15. Vemula, R.R., Kothare, M.V., Sircar, S.: Anatomy of a rapid pressure swing adsorption process performance. AIChE J. **61**(6), 2008–2015 (2015)
16. Moran, A., Patel, M., Talu, O.: Axial dispersion effects with small diameter adsorbent particles. Adsorption **24**(3), 333–344 (2018)
17. Vemula, R.R., Sircar, S.: Comments on the reliability of model simulation of a rapid pressure swing adsorption process for high-purity product. Ind. Eng. Chem. Res. **56**(31), 8991–8994 (2017)
18. Ruthven, D.M.: Principles of Adsorption and Adsorption Processes. Wiley, New York (1984)
19. Haghpanah, R., Majumder, A., Nilam, R., Rajendran, A., Farooq, S., Karimi, I.A., Amanullah, M.: Multiobjective optimization of a four-step adsorption process for postcombustion CO_2 capture via finite volume simulation. Ind. Eng. Chem. Res. **52**(11), 4249–4265 (2013)
20. Rajendran, A., Kariwala, V., Farooq, S.: Correction procedures for extra-column effects in dynamic column breakthrough experiments. Chem. Eng. Sci. **63**(10), 2696–2706 (2008)
21. Wakao, N., Funazkri, T.: Effect of fluid dispersion coefficients on particle-to-fluid mass transfer coefficients in packed beds: correlation of sherwood numbers. Chem. Eng. Sci. **33**(10), 1375–1384 (1978)
22. Pini, R., Joss, L., Hejazi, S.A.: Quantitative imaging of gas adsorption equilibrium and dynamics by X-ray computed tomography. Adsorption **15**, 1–18 (2020)
23. Mazzotti, M., Rajendran, A.: Equilibrium theory—based analysis of nonlinear waves in separation processes. Annu. Rev. Chem. Biomol. Eng. **4**, 119–141 (2013)
24. Giese, M., Rottschäfer, K., Vortmeyer, D.: Measured and modeled superficial flow profiles in packed beds with liquid flow. AIChE J. **44**(2), 484–490 (1998)

Publisher's Note Springer Nature remains neutral with regard to jurisdictional claims in published maps and institutional affiliations.